The Astrophysical Journal, 610:762–771, 2004 August 1

A SOFT X-RAY EXCESS IN THE A754 CLUSTER

Mark J. Henriksen,[1] Daniel S. Hudson, and Eric Tittley
Joint Center for Astrophysics, Department of Physics, University of Maryland in Baltimore County, 1000 Hilltop Circle, Baltimore, MD 21250
Received 2003 June 11; accepted 2004 March 3

ABSTRACT

We have analyzed the *Chandra*, *BeppoSAX*, *ASCA*, and *ROSAT* PSPC observations of A754 and report evidence of a soft, diffuse X-ray component. A radial analysis shows that it is detected within a region that extends out to 8′ from the X-ray center and that the emission is higher in the central region of the cluster. Fitting a thermal model to the combined *BeppoSAX* and PSPC spectra show excess emission below 1 keV in the PSPC and above 100 keV in the *BeppoSAX* PDS. The source, 26W20, is in the field of view of the PDS. The addition of a power law, with the spectral parameters measured by Silverman et al. in 1998 for 26W20, successfully models the hard component in the PDS. The excess soft emission can be attributed to a low-temperature, 0.77–1.21 keV, component. The soft excess is also modeled with a power law, although the 90% uncertainty for the normalization of the power law is consistent with zero. Either component added to a hot thermal component provides a statistically significant improvement over a single hot thermal component. The *Chandra* temperature map provides a detailed description of the thermal state of the gas on a scale of 100 kpc and larger and does not show any region cooler than 5.9 keV (90% confidence) within the region where the cool component was detected. Calculations of the expected emission from one or more groups randomly embedded in a hot gas component were performed that demonstrate that groups are a plausible source of ~1 keV emission, in that they can match the measured cool-component luminosity without violating the spatial temperature constraints provided by the temperature map. The cool component is centrally peaked in the cluster, and the gas density and temperature are relatively high, arguing against the warm hot intergalactic medium as the source of the X-ray emission. Furthermore, because the cool component is centrally peaked, the groups are likely embedded in the intracluster gas, rather than in the intercluster gas. The typical X-ray emission from early-type galaxies is not high enough to provide the total cool-component luminosity, 2.1×10^{43} ergs s^{-1}. The peak of the cool component is located between the low-frequency radio halos, thus arguing against a nonthermal interpretation for the emission based on the synchrotron inverse Compton model, which requires that the nonthermal X-ray and radio emission be cospatial. Thus, we conclude that emission from embedded groups is the most likely origin of the cool component in A754.

Subject headings: galaxies: clusters: individual (A754) — X-rays: galaxies: clusters

1. INTRODUCTION

Mergers appear to be commonly occurring in galaxy clusters, judging by the large amount of substructure seen in their X-ray and optical morphologies. Signatures of an active merger are seen directly in temperature maps prepared from X-ray observations or indirectly in nonthermal radio and X-ray emission from cosmic-ray electrons accelerated at the shock front formed by the merger. A merger in A754 was inferred from modeling the integrated *HEAO 1* and *2* X-ray spectrum with two temperature components in the approximate temperature ratio of 3 : 1 (Henriksen 1993). *ASCA* observations resolved the spectral components into a temperature map (Henriksen & Markevitch 1996) with modest resolution (5′ square regions). They found that several regions were hotter than the average cluster temperature and inferred that they were shocked gas from the merger. Comparison of the pattern of shocked gas simulations suggested a major, off-center merger (Henriksen & Markevitch 1996). Similar temperature structure was also seen in the *ROSAT* temperature map (Henry & Briel 1995). Optical observations showed subclustering in the galaxy distribution, providing further evidence of the merger (Zabludoff & Zaritsky 1995). In an analysis of the *Chandra* observation, the possibility that A754 has had several mergers has been raised by Markevitch et al. (2003). Low-frequency radio observations (Kassim et al. 2001) have uncovered two regions of extended radio emission with an estimated spectral index that is consistent with a steep-spectrum source. The radio observations show that the western radio halo is spatially located at the hottest cluster region seen by *ASCA*, suggesting a connection between the shocked gas and cosmic-ray acceleration. Simulations of cosmic-ray acceleration in a cosmological setting (Miniati et al. 2001) predict that the nonthermal X-ray and radio emission should be contemporaneous. However, nonthermal X-ray emission is difficult to detect, because the power law is steep and therefore provides considerably less emission in the hard X-ray band than in the soft X-ray band. In the hard X-ray band (>25 keV), although the spectrum should be free of the thermal cluster emission, currently only large–field of view, nonimaging detectors are capable of detecting the nonthermal component. Thus, it is necessary to account for the effect of contamination by nonthermal emission from active galactic nuclei (AGNs) in these nonimaging observations. In the soft X-ray band, one must accurately model the thermal components, which are generally not single-phase in the cluster center, in order to measure the nonthermal component. Both approaches have been utilized extensively by authors reporting on nonthermal X-ray measurements from clusters.

[1] Also at Laboratory for High Energy Astrophysics, NASA Goddard Space Flight Center, Greenbelt, MD 20771.

Cluster soft X-ray spectra are often better fitted by two components. This result is found for a number of clusters and across a wide range of data sets, including those with low spatial resolution: (1) with *BeppoSAX*, IC 1262 (Hudson et al. 2003), A3560 (Bardelli et al. 2002), and A85 (Lima Neto et al. 2001); (2) with *ROSAT*, MKW 4S, AWM 5, and NGC 6329 (Dahlem & Thiering 2000); (3) with *RXTE* and *ASCA*, Coma, A2319, and A2256 (Gruber & Rephaeli 2002; Rephaeli & Gruber 2002; Henriksen 1999, respectively); (4) with *RXTE* and *ROSAT*, A1367 (Henriksen & Mushotzky 2001); (5) and with *ROSAT* and *ASCA*, Hydra A and Centaurus (Ikebe et al. 1997, 1999, respectively). Two-component spectra are found in clusters with a wide range of characteristics, including clusters with both regular and irregular optical morphologies, clusters that appear to be undergoing major mergers or minor accretions, and those both with and without radio halos or relics. Two-component spectral models consist of two thermal components or a single thermal plus a nonthermal component. For some clusters, one of the models may be a better fit to the data than the other, while for other clusters one must rely on physical arguments to determine the correct model.

In this paper, we model the *ROSAT*, *BeppoSAX*, and *Chandra* X-ray observations of the A754 galaxy cluster with thermal and nonthermal models that are well matched to the spatial and spectral capabilities of the data sets. We present evidence of a new, low-temperature component in this cluster and compare its measurements to our calculations of the emission from embedded galaxy groups. A Hubble constant of $H_0 = 65$ km s^{-1} Mpc^{-1} is used throughout this paper.

2. OBSERVATIONS AND ANALYSIS

2.1. *Optical*

A754 is a rich galaxy cluster located at $\alpha, \delta = 09^{\rm h}08^{\rm m}50\overset{\rm s}{.}1$, $-09^\circ 38' 12''$ (J2000.0), with a redshift of 0.0542 (Struble & Rood 1999). A map of the optical galaxy structure (Fig. 1) was prepared for comparison with X-ray and radio structure (Kassim et al. 2001). The galaxy sky surface density was determined for the region surrounding A754. The Digitized Sky Survey (DSS) image of a single Second Epoch Survey *R*-band plate of the region[2] was processed by the source extraction tool, SExtractor.[3] The tool produces a listing of object positions, fluxes, elongations, and FWHMs, among other parameters. The parameters are used to discriminate between galaxies and stars, with galaxies being associated with any object that is particularly dispersed or elongated. The galaxies were selected down to a limiting magnitude of 19 (images are calibrated to 0.5 mag). The threshold for being considered dispersed was an FWHM $> 4''$ (the FWHM of stellar images is $3\overset{''}{.}0$), while an elongation threshold of the long axis being 1.4 times larger than the short was used to minimize possible contamination from stars, since the image PSF (point-spread function) is slightly noncircular. The positions of the extracted galaxies were smoothed by an adaptive kernel to produce a number density field. For each point in the field, the adaptive kernel maintained a constant number of 16 galaxies in the density estimate. The field was then smoothed on a scale, $41''$, equivalent to 50 kpc at the distance of the cluster. Isocontours are at 2 σ intervals above the background levels.

[2] See http://archive.stsci.edu/cgi-bin/dss_plate_finder.

[3] See http://terapix.iap.fr. Follow links to "software products" and "packages."

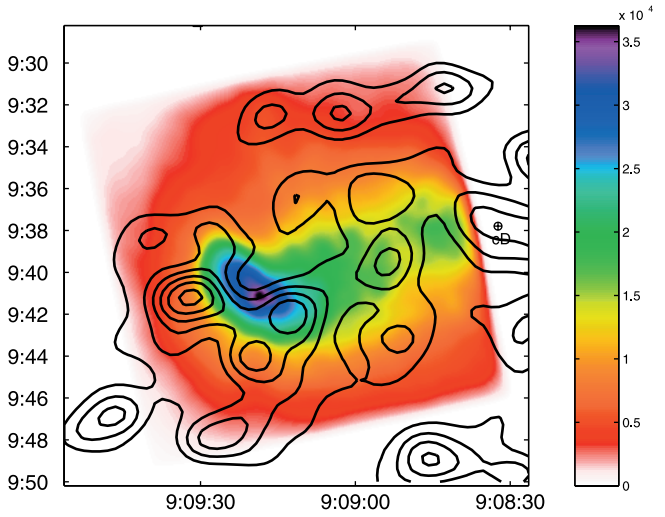

FIG. 1.—Color-coded intensity map of background-subtracted image of the A754 cluster on the ACIS-I array. Galaxy isocontours are at 2 σ intervals above the background level.

2.2. *Chandra*

The A754 galaxy cluster was observed by *Chandra* on 1999 October 30 for 44,700 s. The peak cluster emission is located on chip 1 of the ACIS-I detector, and the elongated emission spans all four chips. The total count rate of the uncleaned data is 18.35 ± 0.02 counts s^{-1}, with a peak of 51 ± 2 counts s^{-1}, which is well below the saturation limit of the ACIS chips operating in faint mode (170 counts s^{-1}). The cleaned data have a count rate of 11.3 counts s^{-1}. Figure 1 is a color-coded surface brightness map that shows the full $21' \times 21'$ image in the 0.3–8.0 keV band. The image was obtained using processing routines outlined in the CIAO, version 2.2.1, science threads. Since A754 was observed during a period in which the ACIS temperature was -110°C, it was important to correct the data for the increased charge transfer inefficiency (CTI). This was done with the scripts provided at the CXC (*Chandra* X-Ray Center) Web site. The data were then cleaned for flares and point sources. A background map was created following the CIAO, version 2.2.1, science thread *ACIS Blank-Sky Files*, which utilizes the blank-sky data sets compiled by Maxim Markevitch. The *merge_all* script was used to create an exposure map and an exposure-corrected source image. The background was normalized to the exposure time of the data set, divided by the exposure map, and then subtracted from the exposure-corrected source image. The background-subtracted, exposure-corrected image was then smoothed to form the image seen in Figure 1.

The intensity map is quite complex overall and shows several interesting features. The central peak is elongated along the northeast-southwest direction. The diffuse emission drops off sharply to the east and northeast of the elongated central peak but extends to the west past the edge of the ACIS-I detector. A small second X-ray peak in the diffuse emission is visible on the western edge of the I3 chip.

Spectra were extracted from the cleaned, CTI-corrected ACIS event files to make the temperature map. The redistribution matrix file (RMF) for each region was determined by taking a count-weighted average of the relevant RMFs provided by the CTI team. Since the RMF energy bins varied in size, the CIAO tool *mkwarf* was unable to parse the

RMF energies. Therefore, the ancillary response function (ARF) for a region was created by combining ARFs created using *mkwarf* for each energy range of identical energy bins. The regions analyzed for the temperature map were chosen to maintain a 10% error in the temperature during spectral fitting. A MEKAL model was used with $n_{\rm H}$ frozen at the Galactic value, 4.34×10^{20} cm^{-2}. The abundance, temperature, and normalization were free parameters.

2.3. *BeppoSAX*

BeppoSAX observed A754 on 2000 May 17 with the Medium Energy Concentrator Spectrometer (MECS) for ~121,000 s and the Phoswich Detection System (PDS) for ~55,000 s. MECS data were extracted from regions centered on the *BeppoSAX* pointing (α, $\delta = 09^{\rm h}09^{\rm m}21\overset{\rm s}{.}6$, $-09^\circ 41' 02''$; J2000.0) to facilitate creating proper response matrices and producing proper background PHAs. The MECS has a broad energy band and is used to constrain the diffuse thermal component. An on-axis, circular region with an $8'$ radius was extracted from the MECS2 and MECS3 event files provided from the Italian Space Agency (ASI) archive. ASI also provides an on-axis RMF and an $8'$ background PHA file (taken from blank-sky fields at high Galactic latitude) for MECS2 and MECS3. In order to create an ARF for our $8'$ region of extended emission, we approximated the X-ray emission as radially symmetric. The SAXDAS program *effarea* uses a point-source ARF and a surface brightness profile to produce a MECS ARF for a concentric, on-axis region of radially symmetric, extended emission (Fiore et al. 1999). An on-axis, point-source ARF was obtained from the ASI Web site, and the *ROSAT* High Resolution Imager (HRI) data were used to create the surface brightness profile. Extracting concentric regions for the MECS data is difficult, because extraction must be done in sky coordinates in order to match the MECS regions with the PSPC regions. However, since the background events file is from multiple observations, it is not possible to extract a background PHA file in sky coordinates from the background events files provided at the ASI Web site. We therefore constructed an algorithm that uses the MECS2 and MECS3 source data to convert detector coordinates to sky coordinates. These algorithms produced an error of no more than 3 pixels in sky coordinates for the MECS2 and MECS3 source data, corresponding to an error of $\leq 0\overset{'}{.}4$, which is much smaller than the MECS on-axis 50% encircled energy width of $1\overset{'}{.}25$ at 6.4 keV (Boella et al. (1997). The *effarea* program was then used to create ARFs for each region, with the procedure described above. All model parameters fitted to the MECS2 and MECS3 spectra were tied together, but the data sets were not merged, in order to account for differences in their responses.

PDS event files were obtained from NASA's HEASARC and processed using the standard reduction methods described in Fiore et al. (1999). We obtained the proper PDS RMF from the ASI Web site. Since the PDS is not an imaging instrument, it is impossible to limit the field of view or remove point sources from it. Significant point-source contamination to the PDS spectrum of A754 comes from 26W20. This X-ray–bright radio galaxy is visible in the PSPC at a distance of $24\overset{'}{.}5$ to the southwest of A754's center, well within the PDS's field of view. Silverman et al. (1998) report a total radio flux of 435 ± 40 mJy emitted by core, tail, and lobe components. These authors report an X-ray luminosity measured by the on-axis *ROSAT* HRI observation of $(3.70 \pm 0.10) \times 10^{43}$ ergs s^{-1}. The best-fit model for the emission using the *ROSAT* PSPC is $\alpha = 1.32 \pm 0.17$. Since 26W20 is well outside our PSPC and MECS extraction regions, it does not appear in their spectra; therefore, a power-law component, with a photon index frozen at $\alpha_{\rm X} = 1.3$ and normalization 2.0×10^{-4} photons cm^2 s^{-1} keV^{-1} at 1 keV was included in all of the PDS spectral models but excluded from the spectral models of the other detectors.

2.4. *ROSAT*

In addition to the *Chandra* observation of A754, there are three 1996, nearly on-axis, *ROSAT* Position Sensitive Proportional Counter-B (PSPC) observations (total integrated time of ~16,500 s). The PSPC regions analyzed correspond to that used in the *BeppoSAX* analysis. The PSPC data were reduced using standard FTOOLS, version 5.2. The temporal and spatial gain variations were corrected using the *pctcor* and the in-flight–mode *pcecor* correction algorithms, respectively. The background was extracted from regions far from the source emission. Care was taken to avoid regions obstructed by support structures. We took several steps to produce proper background spectra. First, we used the exposure map, which maps instrument efficiency as well as exposure time, to adjust the *BACKSCAL* keyword in the background spectra to account for the difference in average instrument efficiency between the source and background regions. Next, we used the *pcparpha* tool to determine the particle background for both the source and background regions. The net background is given by

$$\begin{aligned}\text{background}_{\rm net} = &\left(\text{background} - \text{particle}_{\rm bkg}\right) \\ &+ \text{particle}_{\rm src}\left(\text{eff}_{\rm src}/\text{eff}_{\rm bkg}\right)\left(\text{area}_{\rm bkg}/\text{area}_{\rm src}\right).\end{aligned}$$

ARFs were created for each PSPC observation using *pcarf*. The three source and background PHA files for each region were separately summed using *mathpha*. The ARFs for the merged spectra were created by using *addarf* to calculate a count-weighted average of the three individual ARFs from each period of observation. The RMF for the gain-corrected data was obtained from the HEASARC database. Overall, 15 PHA files were extracted to produce five merged PHA files: a merged PHA for an $8'$ circular region centered on the *BeppoSAX* pointing and four merged PHAs for four concentric regions spanning $10'$ in $2\overset{'}{.}5$ intervals. The lack of spatial information in the PDS and the inability to identify point sources in the MECS (due to its relatively large PSF) precludes the removal of point sources; therefore, point sources were not removed from the PSPC data, in order to preserve consistency between the PSPC and *BeppoSAX* spectral files. Since 26W20 is well outside our *ROSAT* extraction region, it was excluded from the spectral models for the PSPC and the MECS detectors, as well.

3. RESULTS

3.1. *Chandra Temperature and Abundance Distribution*

The temperature map (see Fig. 2; region values in Table 1) shows two important features that were previously identified in the temperature map obtained with *ASCA* (Henriksen & Markevitch 1996): hot, 16–20 keV gas (region 2) near the northwestern galaxy component and cooler, ~7 keV gas (regions 15 and 16) north of the southeastern galaxy component (Zabludoff & Zaritsky 1995) and cospatial with the X-ray peak. There is a gradient in the *ASCA* temperature map, running east-west approximately through *Chandra* regions 14, 1, 3, and 2, that is also visible in the *Chandra* map. In addition to a temperature map, spectra were extracted for annular regions

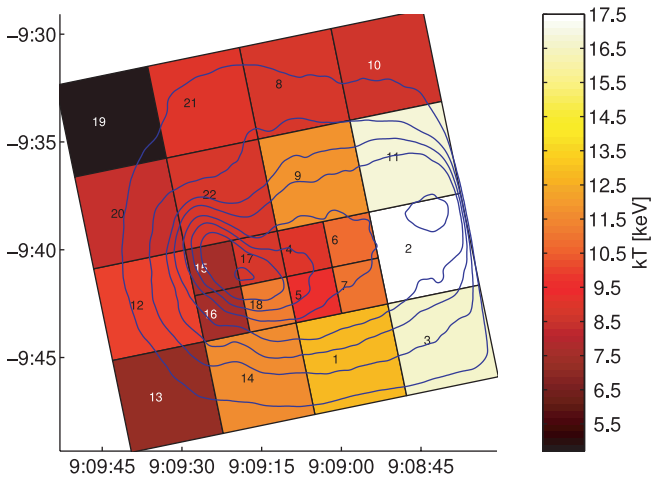

FIG. 2.—Two-dimensional temperature map obtained from the *Chandra* observation. Hot gas is visible to the west of the center and cool gas running across the X-ray peak on the east side.

centered on the *Chandra* peak X-ray flux. Each annulus was chosen so that there were at least 30,000 counts in a region. The data were reduced identically to the data for the temperature map. Figure 3 shows the results from the annuli. The radial profile becomes dominated by gas to the west of center at radii greater than $\sim 4'$ and clearly confirms that the temperature increases across the cluster from east to west by nearly 50%, similar to the ridge structure visible in the *Chandra* and *ASCA* temperature maps. Within $\sim 4'$, the temperature decreases as a result of the contribution from regions 15, 16, 20, and 22, which contain gas that is below the average cluster temperature. Comparison of our temperature map with similar regions analyzed in Markevitch et al. (2003) shows excellent agreement.

TABLE 1
SPECTRAL FITS OF REGIONS

Region	kT_1 (keV)
1	$12.70^{+1.41}_{-1.16}$
2	$17.40^{+1.85}_{-1.42}$
3	$16.70^{+2.95}_{-2.03}$
4	$8.99^{+0.85}_{-0.71}$
5	$9.60^{+1.06}_{-0.86}$
6	$10.80^{+1.28}_{-1.04}$
7	$11.20^{+1.6}_{-1.24}$
8	$8.54^{+1.11}_{-0.9}$
9	$11.60^{+1.05}_{-0.82}$
10	$8.36^{+1.74}_{-1.18}$
11	$16.70^{+1.93}_{-1.46}$
12	$9.73^{+1.11}_{-0.93}$
13	$6.76^{+1.18}_{-0.91}$
14	$11.6^{+1.44}_{-1.15}$
15	$7.49^{+0.55}_{-0.46}$
16	$7.52^{+0.69}_{-0.61}$
17	$8.66^{+0.69}_{-0.59}$
18	$11.3^{+1.28}_{-0.96}$
19	$4.56^{+0.84}_{-0.65}$
20	$8.12^{+1.06}_{-0.84}$
21	$8.70^{+1.16}_{-0.94}$
22	$8.55^{+0.61}_{-0.53}$

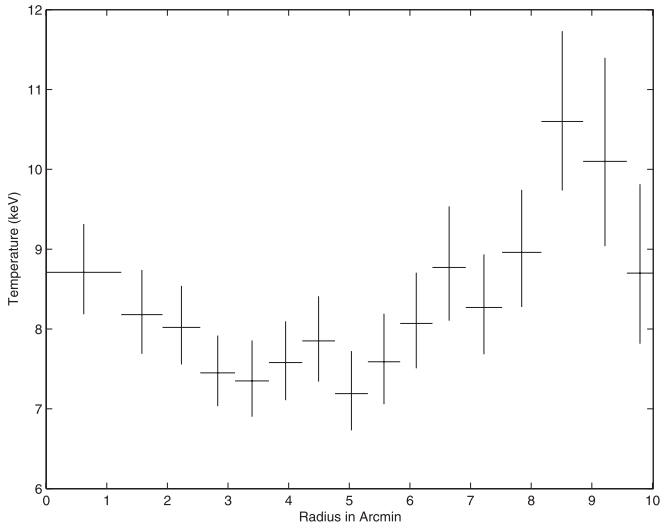

FIG. 3.—Radial temperature profile obtained from *Chandra* observations, consistent with the temperature map in showing that the temperature generally increases across the cluster from east to west. There are 30,000 counts per region.

The radial abundance profile obtained from jointly fitting MECS and PSPC spectra from the same annular regions is shown in Figure 4. Using both the MECS and PSPC spectra provides better azimuthal coverage of the cluster and better constrains the radial abundance than does the *Chandra* observation. The radial profile is generally consistent with a constant abundance value of 30% of solar, the global value reported in Table 2. The 90% uncertainties of the outer two abundance measurement points do not quite overlap, suggesting that higher abundance gas may have been dumped during the merger. There is no gradient near the X-ray peak.

3.2. *Soft X-Ray Emission from Embedded Galaxy Groups*

A large region of the *BeppoSAX* MECS and *ROSAT* PSPC images was selected for analysis to search for nonthermal

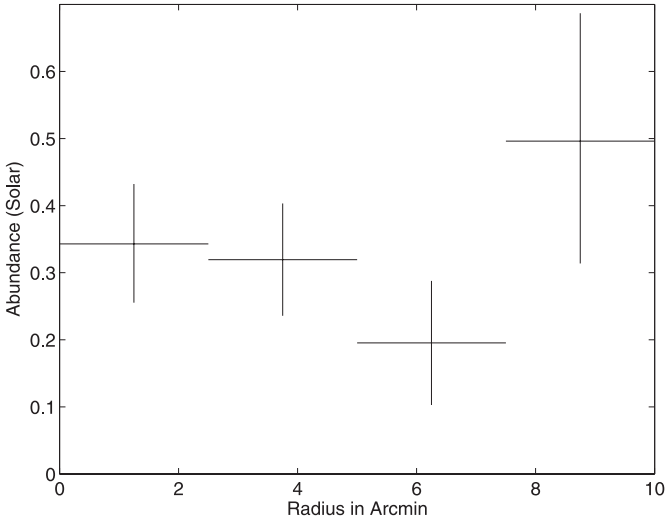

FIG. 4.—Abundance enhancement seen $8'$ from the center of the main (southeastern) cluster, perhaps due to the subcluster involved in the merger. The radial profile is centered on the X-ray peak and obtained from *ROSAT* and *BeppoSAX* observations.

TABLE 2

ROSAT AND *BeppoSAX* SPECTRAL FIT OF 8′ REGION

Model[a]	kT_1 (keV)	Abundance (solar)	kT_2 (keV)	Γ_X	Normalization[b] kT_1 (10^{-2})	Normalization[b] kT_2 (10^{-2})	Normalization[c] Γ_X (10^{-2})	n_H (10^{20} cm^{-2})	χ^2/dof
MEKAL[d]	10.8 ± 0.4	0.28 ± 0.04	...	...	4.99 ± 0.05	...	...	3.9 ± 0.6	495.1296/374
MEKAL	$10.4^{+0.4}_{-0.3}$	0.29 ± 0.04	...	...	5.01 ± 0.05	...	...	4.1 ± 0.6	463.6772/373
MEKAL+power law	10.5 ± 0.4	0.29 ± 0.04	...	$2.2^{+>7.8}_{->5.2}$	$4.93^{+0.13}_{-0.29}$	...	$0.03^{+0.07}_{-0.03}$	4.34[e]	462.9922/372
MEKAL+MEKAL	$10.7^{+0.5}_{-0.4}$	0.29 ± 0.04	$0.97^{+0.24}_{-0.20}$	...	$4.95^{+0.06}_{-0.08}$	$0.20^{+0.13}_{-0.09}$	...	4.34[e]	443.5565/372

[a] All models include photoelectric absorption using Wisconsin cross sections.

[b] $\{10^{-14}/4\pi[D_A(1+z)]^2\} \int n_e n_H \, dV$.

[c] In units of photons cm^{-2} s^{-1} keV^{-1} at 1 keV.

[d] No power law included in PDS to account for 26W20.

[e] Frozen at the Galactic value.

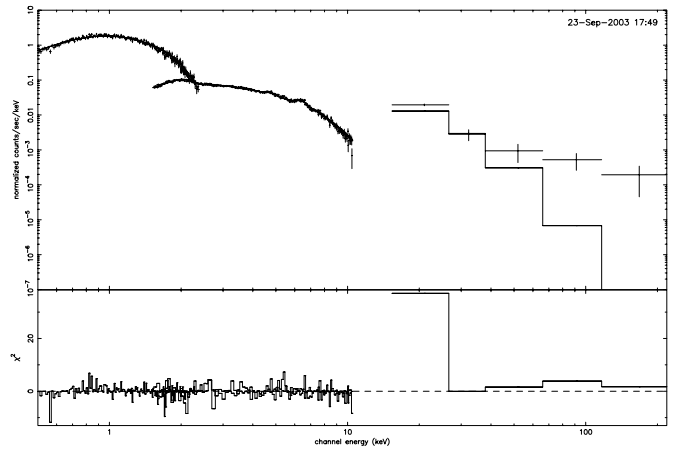

FIG. 5.—Thermal model showing residual hard emission in the PDS.

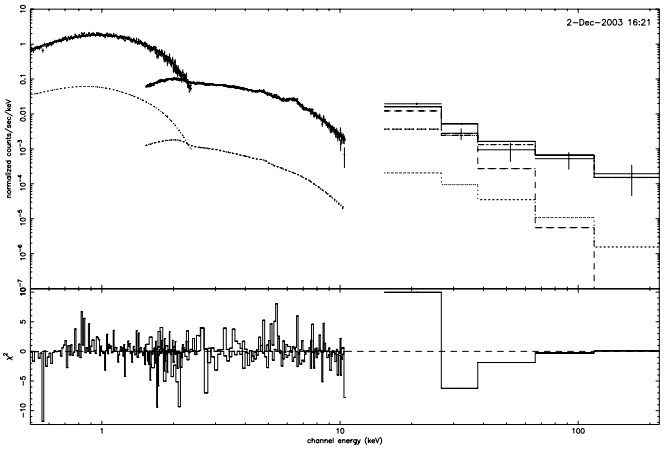

FIG. 7.—Thermal model with two power laws (the second added to model diffuse nonthermal emission). The thermal component is shown by the dashed line, the point source by the dot-dashed line, and the nonthermal component by the dotted line.

X-ray emission. These instruments provide broadband coverage that is able to constrain the cluster components: 0.5–2.0 keV (PSPC), 1.5–10.0 (MECS), and 15–200 keV (PDS). Together they offer a broad energy band of 0.5–200 keV with reasonable signal-to-noise ratio and good spatial resolution up to 10.0 keV. For a hot cluster such as A754, the thermal components will dominate these spectra, and the PDS is crucial for detecting the nonthermal component at high energy. However, the PDS is most sensitive to flat-spectrum emission, which is more typical of AGNs than diffuse emission. The PSPC may be sensitive to the steeper power law that characterizes diffuse nonthermal emission, a component that may dominate the spectrum at low energy.

The results obtained from fitting these data with various single and multiple thermal and nonthermal models are given in Table 2. For the more complex models, the column density was fixed at the Galactic value to reduce the number of free parameters, after single-temperature model fits showed that it is within 5%–10% of the Galactic value. The sequence of Figures 5–8 show data, model, and residuals for progressively more complex models. Figure 5 shows a single MEKAL model fit to the data. Significant residual emission appears around 100 keV and below 1 keV. The PDS field of view contains the BL Lac object 26W20.

Modeling 26W20 in the PDS with the parameters from Silverman et al. (1998)—photon index frozen at $\alpha_X = 1.3$ and normalization 2.0×10^{-4} photons cm^{-2} s^{-1} keV^{-1} at 1 keV—removes the high-energy residuals (Fig. 6). Thus, we do not confirm the detection of a diffuse hard component found by Fusco-Femiano et al. (2003). The remaining soft residuals can be modeled by adding either a nonthermal component (Fig. 7) or a second thermal component (Fig. 8). The parameters determined from these fits are given in Table 2. The second component is not well modeled as nonthermal emission, since the addition of a power law does not significantly improve the fit. The second, diffuse emission component can be modeled as thermal emission with temperature 0.77–1.21 keV and luminosity 2.1×10^{43} ergs s^{-1}, which is 2.3% of the hot thermal component. All luminosity comparisons are bolometric (0.01–100 keV). As can be seen in Table 2, the additional thermal component reduces the total number of degrees of freedom by 1 and reduces χ^2 by 20, so that it is significant with greater than 99.9% confidence using the *F*-test. Thus, the two-component thermal model provides the best fit to the data. As noted in § 2.2, the X-ray contour map shows a possible source in the hottest region of the temperature map, region 2. We fit

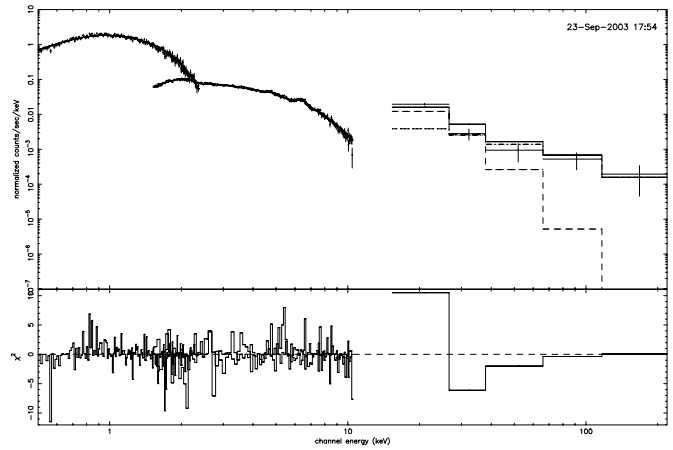

FIG. 6.—Thermal model with power law added to model contaminating source, 26W20, in the PDS. The thermal component is shown by the dashed line and the point source by the dot-dashed line.

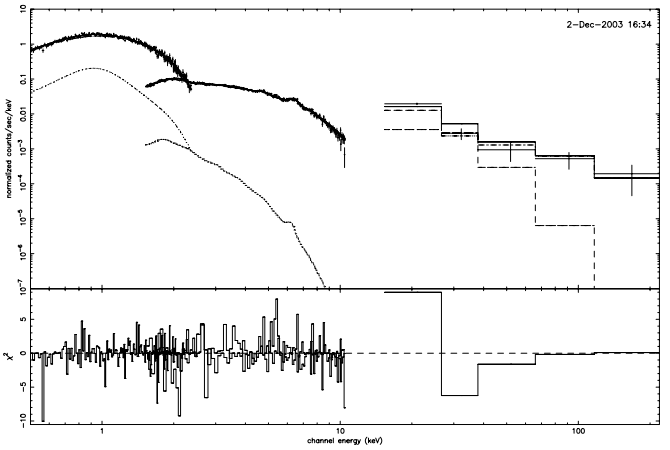

FIG. 8.—Two thermal models with a power law. The first thermal component is shown by the dashed line, the point source by the dot-dashed line, and the second thermal component by the dotted line.

this region with a power law to test if this region is the source of a nonthermal point source. The thermal component is statistically a much better fit to the data. A power law only gives a comparable fit to the thermal model if the column density is allowed to be 3 times the Galactic value. In this case, the spectral index is 1.5–1.55, comparable to that of an AGN. As there are not strong Fe Kα residuals apparent in the power-law fit, we cannot rule out that the region is dominated by an absorbed power-law source rather than hot gas. However, this source does not appear as a nonthermal component when the larger cluster region is analyzed. We fit the above data, including *ASCA* GIS observations, and find that all parameters are consistent, with 90% confidence, with the values in Table 2, except for the column density. The fitted column density, including *ASCA*, decreases so that the 90% uncertainty no longer overlaps with the Galactic value. The large column density is due to incomplete charge collection.

Henriksen & Silk (1996) suggested that the integrated emission from gas associated with several early-type galaxies or groups within the observed region of the cluster may give rise to a 1 keV component. A number of small-scale structures exist in the A1367 cluster that are significantly cooler (0.3–0.9 keV) than their surroundings (3–4.5 keV) (Sun & Murray 2002), suggesting that the early-type galaxy coronae can survive in the intracluster medium (ICM). There are also several similar compact sources not identified with galaxies in that cluster. The dominant elliptical galaxies in the central region of the Coma Cluster retain their coronae and have a temperature of $\sim$1 keV (Vikhlinin et al. (2001). We perform calculations that will test the hypothesis that embedded galaxy groups can give the cool component in A754. This involves making a simulated temperature map with both cluster and group emission for comparison with our *Chandra* temperature map. The *Chandra* temperature map maintains approximately 6000 counts per region to allow spectral fitting of each region. The smallest regions are then $2' \times 2'$, and the largest are $4' \times 4'$. At the redshift of A754, $1' = 73$ kpc.

Calculations were performed of the emission-weighted temperature from embedded groups with pixels similar in size to the pixels in a *Chandra* temperature map. The simulations assume X-ray emission from identical groups (e.g., a similar temperature of 0.97 keV and luminosity equal to the total cool component divided by the number of groups). The groups are embedded randomly in a region $876 \times 876 \times 1000$ kpc, which approximates the region of the *ROSAT*/*BeppoSAX* analysis that yielded the cool component. A square region was chosen to facilitate the random placement of groups. Because of the relatively large extent of the group intergalactic medium, this approximation does not introduce any significant inaccuracy. The short side dimension of the simulated region corresponds to the side of the square inscribed in the circular region of the *ROSAT*/*BeppoSAX* cool-component detection. The depth of the simulated cluster, 1 Mpc, approximates the visible extent of the X-ray emission in the *ROSAT* PSPC image (Henriksen & Markevitch 1996). The group X-ray emission is described by a beta model with beta fixed at 0.5, the core radius allowed to span a range of values that includes groups with very peaked and very flat distributions, and a central density for the groups determined from the luminosity within 250 kpc, a typical radius observed for group emission (Mulchaey et al. 1996). The luminosity for a group is observationally constrained, since it must be equal the total cool-component luminosity divided by the number of groups. The parameters for the A754 cluster gas are as follows: The central density is

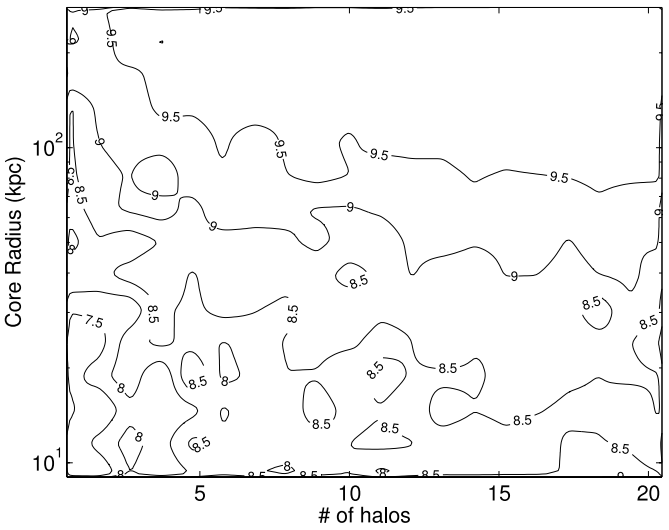

FIG. 9.—Contour plot of minimum simulated temperature map region temperature for combinations of group number vs. core radius. The total emission from the groups, in each case, is set equal to the soft X-ray component. Models with a few luminous groups or many low-luminosity groups are found to give simulated temperature maps that do not violate the observed *Chandra* temperature map.

1.85×10^{-3} cm^{-3} (Abramopoulos & Ku 1983), and the emission-weighted temperature is 10 keV. Because the X-ray emission is highly asymmetric, we approximate the surface brightness distribution as a beta model with beta = $\frac{2}{3}$ and core radius = 300 kpc. Model-fitting the surface brightness profile of rich clusters shows that beta is typically $\frac{2}{3}$ (Jones & Forman 1984) and that X-ray core radii are well constrained to the range of 0.25–0.35 Mpc (Henriksen 1994). We produced a temperature map by embedding two or more groups in the simulated cluster region. The groups range from small, 10 kpc core radius, to large, 100 kpc. While groups are observed with core radii larger than 100 kpc, our calculations show that they do not significantly lower the temperature of the given regions (see Fig. 9); therefore, we do not consider the larger core radii groups in our calculations. We also did not look at the case of more than 20 small halos, because this becomes unphysical for the following reason. Groups with significant X-ray emission contain at least one early-type galaxy. Thus, many small groups mean many early-type galaxies. As discussed below, early-type galaxies alone are not luminous enough to provide the entire cool component. If one requires that the early-type galaxies have a luminosity comparable to that of groups, then the luminosity function is violated. Embedding a single, luminous, cool group or several less luminous groups will change the emission-weighted temperature of the region that the groups are in. Large–core radii groups may affect more than one region, and groups located farther from the center of the cluster will have a more significant effect on the emission-weighted temperatures that are measured. Figure 9 shows the lowest temperature of any region in the simulated temperature maps for the range of group core radii and number of groups tested. We find that for the full range of core radii and number of groups, the lowest temperature observed for any region in the simulated map is well above the 90% confidence observed minimum in the *Chandra* map, 5.9 keV (region 13). Thus, either a small number of luminous groups or many low-luminosity groups can reproduce the cool component and not violate the *Chandra* temperature map. Since the expected emission from galaxy groups can give the cool-component

luminosity and does not violate the constraints imposed by the temperature map, we conclude that groups are a plausible source of the cool component. There are other possible sources for cool thermal gas, including galaxies and intercluster gas, which are addressed in the discussion section.

4. DISCUSSION

In the temperature map that we have prepared, the cooler regions are consistent with the temperatures for those regions measured with *ASCA*. However, the *Chandra* map shows that the cooler gas (regions 15 and 16 in the temperature map) is spatially coincident with a sharply delineated "peanut-shaped region" in the surface brightness map. The low-frequency radio image (Kassim et al. 2001) shows two distinct, high-intensity regions: the small radio region to the east of the X-ray peanut and the large radio region that lies to the west. The peanut appears to be a cool, low-pressure region sandwiched between the radio-emitting regions. The complementary shape of the contours of the peanut morphology and the radio halo suggest that it may be formed, in part, by the pressure exerted on it by the surrounding radio regions. The radio regions are hotter than the surrounding cluster atmosphere, which is consistent with the hypothesis that cosmic-ray acceleration occurs at the shock front. Under the simplest assumption, that primary cosmic-ray electrons are accelerated at the shock front and then propagate out until they radiate their kinetic energy via the inverse Compton process, the electrons do not travel very far, $\sim$10 kpc. Thus, the proximity of the radio emission to the shocked gas is consistent with the simplest model of nonthermal emission by primary cosmic rays. Miniati et al. (2001) found that the proton cosmic-ray pressure may be up to 45% of the thermal gas pressure in clusters. Thus, the proton pressure may be an important contribution to the dynamics of the cluster atmosphere when it expands into gas that is significantly cooler than the ambient cluster gas.

Monotonically decreasing metallicity gradients typically anticorrelate with cluster mergers (De Grandi & Molendi 2001). Thus, a merger acts to mix the gas and erase this type of preexisting gradient. In the case of A3266 (Henriksen & Tittley 2002), an off-center abundance enhancement was found, as opposed to a gradient. In A3266, it appears from the geometry of the merger that the enhancement results from deposition and heating of higher abundance gas during the merger. Similarly, the outer annular region that shows an abundance enhancement in A754 could also be due to deposition of higher density gas during the merger. An off-center abundance profile is more difficult to detect with high significance because the emission integral is $\sim n^2$ and the gas density, n, is typically $\sim r^{-2}$ outside of the cluster core. Thus, the emission integral at 4 core radii is a factor of $\sim$250 lower than that in the center (for an equal volume). Nevertheless, off-center abundance profiles, as in A3266 and A754, may be an important diagnostic for cluster evolution, providing clues to the merger history. Another suggestion is that formation of a metallicity gradient in galaxy clusters may depend more on the presence of a central cD galaxy than on cluster richness (Umetsu & Hattori 2000). The cD galaxy in A754 does not lie near the X-ray peak but lies near the northwestern galaxy clump (see Fig. 1). The proximity of the cD galaxy to the northwestern galaxy peak suggests that the cD galaxy is identified with the northwestern subcluster, located near the hottest region of the cluster. However, it does not appear to be identified with the high-abundance region, as it is not cospatial with this region.

We have presented evidence of a soft X-ray component (0.5–1 keV) that can be successfully modeled by the emission from the intergalactic medium of one or more groups embedded in the ICM. Early-type galaxies have a hot gaseous halo at 1 keV (Forman et al. 1985), comparable to groups, but also typically contain less gas. A King model for A754 parameters (Abramopoulos & Ku 1983) using a central surface density of galaxies of 92 Mpc^{-2} and a core radius of 0.71 Mpc gives an estimate of 75 galaxies within the circular region with radius of 582 kpc. The X-ray and optical core radii should be the same for a hydrostatic model. The X-ray core radius is always better determined statistically, so we use it here. The galaxies identified in a cluster at the redshift if A754 are heavily weighted toward the central region of the cluster because that is the region of highest surface brightness. The number counts within an Abell radius are therefore a reasonable approximation to the central galaxy surface brightness.

The typical fraction of early-type galaxies in rich clusters is 80% (Butcher & Oemler 1978). This would give 59 early-type galaxies. If galaxies provide the cool component, an average L_X is 3.5×10^{41} ergs s^{-1} per early-type galaxy. The distribution of normal early-type galaxies (Eskridge et al. 1995) shows that 10^{41} ergs s^{-1} is typical, so normal, early-type galaxies are unlikely to provide the X-ray emission. Thus, it is less plausible that this large cool component is only from early-type galaxies, and it must involve more X-ray–luminous groups.

Another possibility is a diffuse baryonic halo surrounding the cluster. Several different authors, using different data sets, have reported evidence of a diffuse component in the 0.5–1 keV range . Henriksen & White (1996), using *HEAO 1* and *Einstein* Solid State Spectrometer (SSS) data with a similar broadband coverage to these data but with much lower effective area, reported 0.5–1 keV gas beyond the canonical cooling flow region, contained within the SSS field of view, in several clusters. This gas could be intercluster or from embedded groups. The lack of imaging capability in those data only allowed exclusion of a central cooling flow as the source of the gas. Kaastra et al. (2003) report a soft X-ray component in 5 of 14 galaxy clusters that is visible as an excess in the 0.4–0.5 keV range in the outer cluster atmosphere and is attributed to the warm hot intergalactic medium (WHIGM). Bonamente et al. (2002) report evidence of a diffuse baryonic halo around the Coma Cluster that extends to 2.8 Mpc. Their spectral analysis of *ROSAT* PSPC observations shows that the radial temperature profile of this component is consistently 0.25 keV, with 10% uncertainty. This suggests that the intercluster component is substantially cooler than the A754 soft component, since the temperature of our component is higher than 0.25 keV. Nevalainen et al. (2003) report soft excesses in *XMM* observations of Coma, A2199, A1795, and A3112 in the clusters' inner 0.5 Mpc, a region similar to that covered by our MECS/PSPC analysis. The characteristic temperature is 0.6–1.3 keV, which is also consistent with that of the A754 cool component. They point out that their density, 10^{-4} to 10^{-3} cm^{-3}, is well above that expected from the WHIGM (Davé et al. 2001) projected into the core region of the cluster, making that interpretation unlikely. The average density of the A754 cool component in the cluster core ($0'$–$4'$) is 5.6×10^{-4} cm^{-3}, similarly high compared to that of the WHIGM. Thus, the soft *XMM* components may be consistent with embedded galaxy groups.

The PSPC observations provide some spatial information on the soft-component distribution. Figure 10 shows a radial

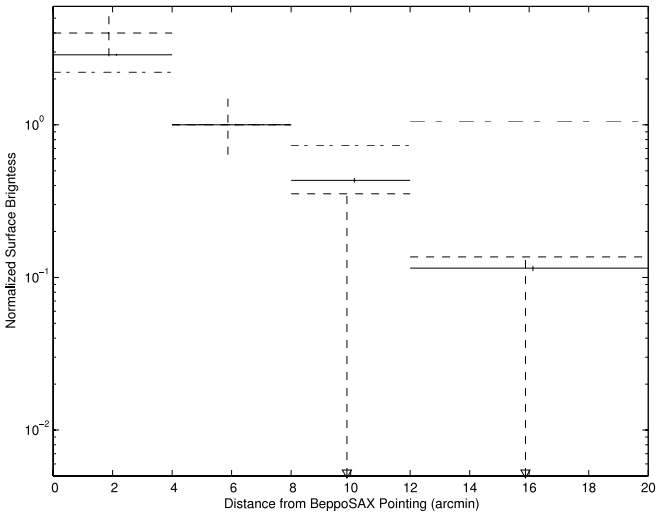

FIG. 10.—Radial surface brightness of the cool (*dashed lines*), hot (*solid lines*), and galaxy (*long-dash–short-dashed lines*) components. The cool component appears to be slightly peaked in the central region relative to the hot component, however, and it is not flat, as would be expect for a projected intercluster component.

surface brightness distribution of the cool, hot, and galaxy components. The soft component extends out to 8′ and is slightly peaked in the center relative to the hot component. The *BeppoSAX* pointing is used as the center of the distributions and lies 45″ to the west of the X-ray peak. The galaxy distribution from the DSS is shown for comparison. It is interesting that the soft X-ray emission is not flat, as would be expected if it were projected emission from filamentary gas surrounding the cluster.

In addition, the highest region of soft emission is located between the regions of radio emission. In the simplest model for nonthermal emission, in which the radio emission is from the synchrotron process and the nonthermal X-ray emission is from the inverse Compton process, the radio and X-ray emission is cospatial. Thus, if the soft component is nonthermal, that would require that the magnetic field be very nonhomogeneous in the cluster, so that the visible radio regions are only where the magnetic field is highest. This interpretation is somewhat unsatisfactory, because if the magnetic field is "frozen in" to the gas, then the region with compressed gas, in the center, must also have the highest magnetic field. This is the opposite of what is required by the location of the radio source. In the absence of nonthermal X-ray emission, one could explain the absence of radio emission in the center as synchrotron aging due to a higher magnetic field in the high-density, central region. However, simulations also show that radio emission should be contemporaneous with nonthermal X-ray emission, which we did not detect. On the basis on our calculations, the best explanation for the origin of the detected soft component is emission from galaxy groups embedded within the hot ICM.

The results of our analysis of the various X-ray data sets bring together new details of a dramatic cluster merger in A754. Above, we presented evidence of temperature structure in the ICM that we attribute to shock heating during a merger. The radio structure of A754 is complex, in that there are two extended features near the X-ray and optical cluster centers. The western radio halo appears to be the result of shock acceleration at the shock front during a major merger, as it is coincident with the hottest gas regions in the cluster. Simulations of cluster merger (Takizawa & Naito 2000) trace the spatial distribution and time evolution of synchrotron radiation due to electrons accelerated at the shock fronts that form during a cluster merger. The morphology of the radio halo and its observed location relative to the shocked cluster gas depend on the viewing angle relative to the merger axis and the age of the merger. When viewed perpendicular to the merger axis, the radio and thermal X-ray have different spatial relationships at different times in the merger. The shocked gas that is west of the cluster center is cospatial with the radio halo. This morphology seems to be consistent with that after maximum contraction, since the simulations show two outward-traveling shocks, with the radio and shocked gas cospatial. While viewing nearly along the line of sight could also account for the shocked gas and radio being cospatial, that viewing angle would also make both regions appear to be in the center of the cluster, which is not the case, since they are west of the center. Thus, we conclude that the merger is in the plane of the sky or at a fairly large angle to the line of sight.

The eastern radio source is not coincident with shocked gas and requires a more complex evolutionary scenario. Since the X-ray peak near the eastern radio source does not appear to be shocked, it is consistent with the simulations of an off-center merger (Roettiger et al. 1998), which was hypothesized on the basis of the *ASCA* temperature map (Henriksen & Markevitch 1996). A band of cool gas running through the center is produced in this scenario. This gas is a mixture of preshocked primary cluster gas and cooler subcluster gas in the simulations and is seen in the temperature map. The eastern radio source may then be from an earlier merger or accretion event, for the following reason. Since radio halo electrons loose their energy as a result of synchrotron emission and have a relatively short lifetime compared with the thermal X-ray component (Takizawa & Naito 2000), the radio halo fades quickly after the most contracting epoch, when the magnetic field is strongest, during the cluster merger. Thus, it would be unlikely for the radio source to still be around after the thermal signs of the merger are gone in the simplest model. However, while it is unlikely, Ohno et al. (2002) find that turbulent Alfvén waves reaccelerate cosmic rays that originated at the shock front, thereby extending the lifetime of the radio halo. The turbulent gas mixing would reduce the thermal signs of the merger. Alternatively, secondary electrons produced by proton-proton collisions followed by pion decay may produce a radio halo with a longer lifetime (Blasi & Colafrancesco 1999). Our hypothesis that the western radio halo is due to primary electrons and the eastern source is due to secondary electrons can be tested by measuring the radio spectral index for each component. The spectral index is predicted to be flatter for secondary than for primary electrons, so a comparison of the spectral indices is a check on our hypothesis.

For the nonthermal X-ray component, our best-fit normalization and Γ, 2.2, give 1.3×10^{14} ergs cm^{-2} s^{-1} keV^{-1} at 20 keV, which is lower than the 90% confidence upper limit reported by Valinia et al. (1999) using *RXTE*, 7.1×10^{14} ergs cm^{-2} s^{-1} keV^{-1} at 20 keV. The upper value, 8.49×10^{14} ergs cm^{-2} s^{-1} keV^{-1} at 20 keV (90% confidence), slightly exceeds the upper limit from the *RXTE*. However, under the simplest assumptions (e.g., a homogeneous magnetic field), the nonthermal soft X-ray component and the radio halo emission should be cospatial, and the fact that the peak of the soft component resides between the radio halos, as discussed in § 3.2, makes a nonthermal origin of the soft X-ray component unlikely. In addition, the 90% flux limit is consistent with zero.

5. CONCLUSIONS

We report on the detection of a soft X-ray component in A754 out to 600 kpc from the cluster center. The cool component peaks near the X-ray center of the A754 cluster and decreases with radius. A thermal model is statistically a much better fit than a nonthermal one for the cool emission. In addition, the peak of the soft component lies between the radio halos, thus making a nonthermal interpretation for the X-ray emission unlikely.

Several potential thermal sources have been evaluated: (1) galaxy coronae embedded in the intracluster medium (ICM), (2) galaxy groups embedded in the ICM, (3) a cD galaxy, and (4) intercluster baryons. While the observed density and temperature of the cool component may be too high to match simulations of intercluster baryons, it is most important that the soft component is peaked in the cluster center and therefore must be trapped in the cluster potential well, thus excluding an intercluster origin. The cD galaxy lies outside of the region where the soft component is detected. Typical galaxy coronae would be required to be a factor of 3–4 more luminous than is observed in surveys of early-type galaxies in order to give the low-energy emission. Thus, early-type galaxies are less likely to be a source of the emission. Our calculations show that one or more groups match the temperature and total luminosity of the soft component and reproduce the low-energy component without violating the *Chandra* temperature map constraints. This remains the most plausible explanation for this new, low-temperature emission. Two temperature components, in which one is typically 1 keV, are often found to provide the best fit to X-ray cluster spectra. We have shown that emission from embedded galaxy groups provides the best explanation for physical origin of this emission in A754 and should be investigated in other clusters.

We thank the referee for valuable comments on this manuscript and the NSF for support through grant AST 96-24716.

REFERENCES

Abramopoulos, F., & Ku, W. H.-M. 1983, ApJ, 271, 446
Bardelli, S., Venturi, T., Zucca, E., De Grandi, S., Ettori, S., & Molendi, S. 2002, A&A, 396, 65
Blasi, P., & Colafrancesco, S. 1999, Astropart. Phys., 12, 169
Boella, G., et al. 1997, A&AS, 122, 327
Bonamente, M., Lieu, R., Joy, M. K., & Nevalainen, J. H. 2002, ApJ, 576, 688
Butcher, H., & Oemler, A., Jr. 1978, ApJ, 226, 559
Dahlem, M., & Thiering, I. 2000, PASP, 112, 148
Davé, R., et al. 2001, ApJ, 552, 473
De Grandi, S., & Molendi, S. 2001, ApJ, 551, 153
Eskridge, P. B., Fabbiano, G., & Kim, D.-W. 1995, ApJS, 97, 141
Fiore, F., Guainazzi, M., & Grandi, P. 1999, Cookbook for *BeppoSAX* NFI Spectral Analysis (Frascati: ASDC), http://www.asdc.asi.it/bepposax/software/cookbook/spectral.html
Forman, W., Jones, C., & Tucker, W. 1985, ApJ, 293, 102
Fusco-Femiano, R., Orlandini, M., De Grandi, S., Molendi, S., Feretti, L., Giovannini, G., Bacchi, M., & Govoni, F. 2003, A&A, 398, 441
Gruber, D., & Rephaeli, Y. 2002, ApJ, 565, 877
Henriksen, M. J. 1993, ApJ, 414, L5
———. 1994, ApJ, 425, 35
———. 1999, ApJ, 511, 666
Henriksen, M. J., & Markevitch, M. 1996, ApJ, 466, L79
Henriksen, M., & Mushotzky, R. 2001, ApJ, 553, 84
Henriksen, M., & Silk, J. 1996, in ASP Conf. Ser. 88, Clusters, Lensing, and the Future of the Universe, ed. V. Trimble & A. Reisenegger (San Francisco: ASP), 213
Henriksen, M. J., & Tittley, E. R. 2002, ApJ, 577, 701
Henriksen, M. J., & White, R. E., III 1996, ApJ, 465, 515
Henry, J. P., & Briel, U. G. 1995, ApJ, 443, L9
Hudson, D. S., Henriksen, M. J., & Colafrancesco, S. 2003, ApJ, 583, 706
Ikebe, Y., Makishima, K., Fukazawa, Y., Tamura, T., Xu, H., Ohashi, T., & Matsushita, K. 1999, ApJ, 525, 58
Ikebe, Y., et al. 1997, ApJ, 481, 660
Jones, C., & Forman, W. 1984, ApJ, 276, 38
Kaastra, J. S., Lieu, R., Tamura, T., Paerels, F. B. S., & den Herder, J. W. 2003, A&A, 397, 445
Kassim, N. E., Clarke, T. E., Ensslin, T. A., Cohen, A. S., & Neumann, D. M. 2001, ApJ, 559, 785
Lima Neto, G. B., Pislar, V., & Bagchi, J. 2001, A&A, 368, 440
Markevitch, M., et al. 2003, ApJ, 586, L19
Miniati, F., Jones, T. W., Kang, H., & Ryu, D. 2001, ApJ, 562, 233
Mulchaey, J. S., Mushotzky, R. F., Burstein, D., & Davis, D. S. 1996, ApJ, 456, L5
Nevalainen, J., Lieu, R., Bonamente, M., & Lumb, D. 2003, ApJ, 584, 716
Ohno, H., Takizawa, M., & Shibata, S. 2002, ApJ, 577, 658
Rephaeli, Y., & Gruber, D. 2002, ApJ, 579, 587
Roettiger, K., Stone, J. M., & Mushotzky, R. F. 1998, ApJ, 493, 62
Silverman, J. D., Harris, D. E., & Junor, W. 1998, A&A, 335, 443
Struble, M. F., & Rood, H. J. 1999, ApJS, 125, 35
Sun, M., & Murray, S. S. 2002, ApJ, 576, 708
Takizawa, M., & Naito, T. 2000, ApJ, 535, 586
Umetsu, K., & Hattori, M. 2000, Adv. Space Res., 25, 617
Valinia, A., Henriksen, M. J., Loewenstein, M., Roettiger, K., Mushotzky, R. F., & Madejski, G. 1999, ApJ, 515, 42
Vikhlinin, A., Markevitch, M., Forman, W., & Jones, C. 2001, ApJ, 555, L87
Zabludoff, A., & Zaritsky, D. 1995, ApJ, 447, L21